CrossMark

RESEARCH ARTICLE

Quantified infrared imaging of ignition and combustion in a supersonic flow

Timothy Ombrello[1] · David L. Blunck[2] · Michael Resor[3]

Abstract The utility of quantified infrared radiation imaging was evaluated through interrogating ignition and burning processes within a cavity-based flameholder in supersonic flows. Two ignition techniques, spark discharge and pulse detonation, along with quasi-steady cavity burning were used to assess the sensitivities of measurements of radiation intensities in the infrared. The shedding of ignition kernels from the spark discharge was imaged, showing that sufficient signal-to-noise ratios can be achieved even with weak radiation emission levels. The ignition events using a pulse detonator were captured with time-resolved measurements of the plume evolution, including the barrel shock, Mach disk, and shock diamonds. Radiation emissions from subsequent firings of the pulse detonator increased, indicating that heat loss to the tube walls occurred in the early pulses. Imaging of the quasi-steady burning within the cavity demonstrated that the highest burning flux (visible broadband chemiluminescence) and radiation from hydrocarbons (3.4 μm) do not coincide with each other for the fueling strategy used. Numerical simulations provided insight into the species distributions that caused the infrared emissions. Overall, infrared radiation measurements have been shown to be feasible through combustor windows in the harsh combustion environments that were interrogated, and offer a new avenue for rapid and quantitative measurements of reactive flow.

List of symbols

I Radiation intensity (W/m^2 sr)
I_b Blackbody radiation intensity (W/m^2 sr)
s Path length (m)
α Absorptivity (–)
κ Linear absorption coefficient (1/m)
λ Wavelength (μm)
τ Transmissivity (–)

1 Introduction

The development of high-speed air-breathing propulsion systems depends upon the ability to understand the complex fluid dynamic and combustion processes involved. Flows within these engines are supersonic, at high temperatures, and are highly turbulent. The interactions involved in and between ignition, flame holding and stabilization at these unique conditions are highly coupled and complex, requiring detailed interrogation in order to elucidate the specific controlling physics. Additionally, the spatial and temporal scales for the processes can be quite disparate, further exacerbating the situation. This has motivated considerable research targeting non-intrusive diagnostics to provide qualitative and sometimes quantitative insights into mixing and combustion. For example, particle image velocimetry (PIV) has been used at both Hz and kHz bandwidth to examine non-reactive and reactive supersonic flow fields (Tuttle et al. 2014; Peltier and Carter 2015). Planar laser-induced fluorescence (PLIF) of NO has been applied to investigate the mixing characteristics of jets in supersonic cross-flows (Lee et al. 1992; Allen et al. 1993; Gruber

✉ David L. Blunck
David.Blunck@oregonstate.edu

1   High Speed Systems Division, Air Force Research Laboratory, 1950 Fifth Street, Wright-Patterson AFB, OH 45433, USA

2   School of Mechanical, Industrial, and Manufacturing Engineering, Oregon State University, 314 Rogers Hall, Corvallis, OR 97331, USA

3   Innovative Scientific Solutions, Inc., 7610 McEwen Rd, Dayton, OH 45459, USA

et al. 2004; Ombrello et al. 2015b). PLIF of OH and CH_2O has been employed to interrogate the turbulent burning processes within supersonic combustors (Allen et al. 1993; Gauba et al. 1997; Gruber et al. 2004; Rasmussen et al. 2005, 2007; Ryan et al. 2009; Do et al. 2010; Cutler et al. 2014). More recently, the application of higher bandwidth (kHz) OH and CH_2O PLIF has provided time-resolved measurements of ignition and burning processes within a cavity-based flameholder (Hammack et al. 2013; Miller et al. 2016). Additionally, tunable diode laser absorption spectroscopy (TDLAS) has been used with one or more lines-of-sight for quantitative temperature and species concentrations measurements in the exhaust of a high-speed combustible flow (Brown and Herring 2012; Busa et al. 2015). While laser diagnostic techniques can provide valuable information, they can also require significant resources for equipment, set-up, and execution. Furthermore, application of some laser diagnostics is not possible for high-speed applications because of limitations in optical access.

High-frame-rate emission-based imaging techniques have been implemented recently to reduce diagnostic resources when studying high-speed reactive flows and still provide insights into the fluid mechanic and combustion processes. To this end, schlieren and shadowgraph imaging have been used to visualize fluid dynamic processes through density gradients. These techniques have been applied at frequencies up to 100 kHz (Ombrello et al. 2015a, b). Additionally, chemiluminescence imaging (visible spectra) has been applied to enable time-resolved visualization of the location of heat release. This provided an unprecedented perspective of the combustion and ignition processes in supersonic flows (Ombrello et al. 2015a, b). While implementation of emission-based techniques tend to be relatively simple and require fewer resources, they typically can be used only to provide qualitative information. Thus, there is a need to consider other emission-based imaging techniques which can be quantitative and readily implemented.

Mid-infrared imaging can provide quantitative measurements of the radiation intensity emitted or absorbed from gases such as H_2O, CO_2, CO, and hydrocarbons. Such measurements have been used to determine turbulent radiation statistics of reacting and non-reacting flows (Blunck et al. 2012b; Rankin et al. 2014), quantify the spatial distribution of combustion products in a flame (Rhoby et al. 2014), determine the temperature in spark kernels (Blunck et al. 2012c), evaluate species concentrations in an exhaust plume (Gross et al. 2010), and estimate the water vapor concentration in a H_2 flame (Blunck et al. 2009). In summary, the quantifiable aspect of infrared thermography allows it to be used to provide insights into the fluid mechanics of reacting and non-reacting flows.

Measured radiation intensities can be used to assess computational fluid dynamics calculations and provide a better understanding of scalar distributions within flows. In one approach, the calculated temperature and species distributions are used to solve the radiative transfer equation (Modest 2003) and determine the radiation intensity for comparison to measurements (Blunck et al. 2012a; Newale et al. 2015). For example, Blunck et al. (2012a) determined that three-dimensional calculations were required to adequately capture mixing and entrainment in an exhaust plume based on comparison of radiation intensity measurements and calculations. Using similar comparisons, Rankin et al. (2015) concluded that including radiation losses are important in simulations even for flames with relatively low radiative heat losses. As a second approach to evaluation, measured radiation intensities can be used to determine scalar distributions without directly calculating the radiation intensities. For example, Chuah et al. (2016) found evidence that extensive fuel pyrolysis occurs within the core of alcohol pool flames based on the distribution of radiation emissions from C–O stretch bands, CO_2, and H_2O. This is in contrast to the common assumption that fuel pyrolysis occurs near the flame sheet from alcohol pool fires. Insight into the scalar distribution is enabled because the radiation intensity depends on the concentration of radiating species, path lengths, and temperatures.

The focus of this effort is to assess the feasibility of infrared imaging of the ignition and combustion processes in a cavity flameholder for a Mach 2 flow, in consideration of the potential advantages of radiation intensity measurements. The goal was to assess whether or not the diagnostic technique could provide quantification like planar laser measurements, but retain the experimental simplicity of emission-based visualization. This effort extended infrared diagnostics from laboratory flames (Blunck et al. 2009; Rankin et al. 2014, 2015; Rhoby et al. 2014) to a more realistic engine environment which included transmission, absorption, and emission through windows. First, these evaluations report measurements of the radiation intensity emitted during a quasi-steady cavity burning process relative to the fueling rate, and hence equivalence ratio. The results were compared to calculated species and temperature distributions to understand what species generated the radiative emissions and the species distributions within the cavity. Second, the cavity ignition processes using two different energy deposition techniques were evaluated using infrared thermography. By using a spark discharge and a pulse detonator (PD) for cavity ignition, infrared imaging was explored for highly transient processes and the sensitivity of the technique evaluated.

Fig. 1 Illustration of the cavity-based flameholder used for the experiments, with demarcation of the top and side camera views through the windows
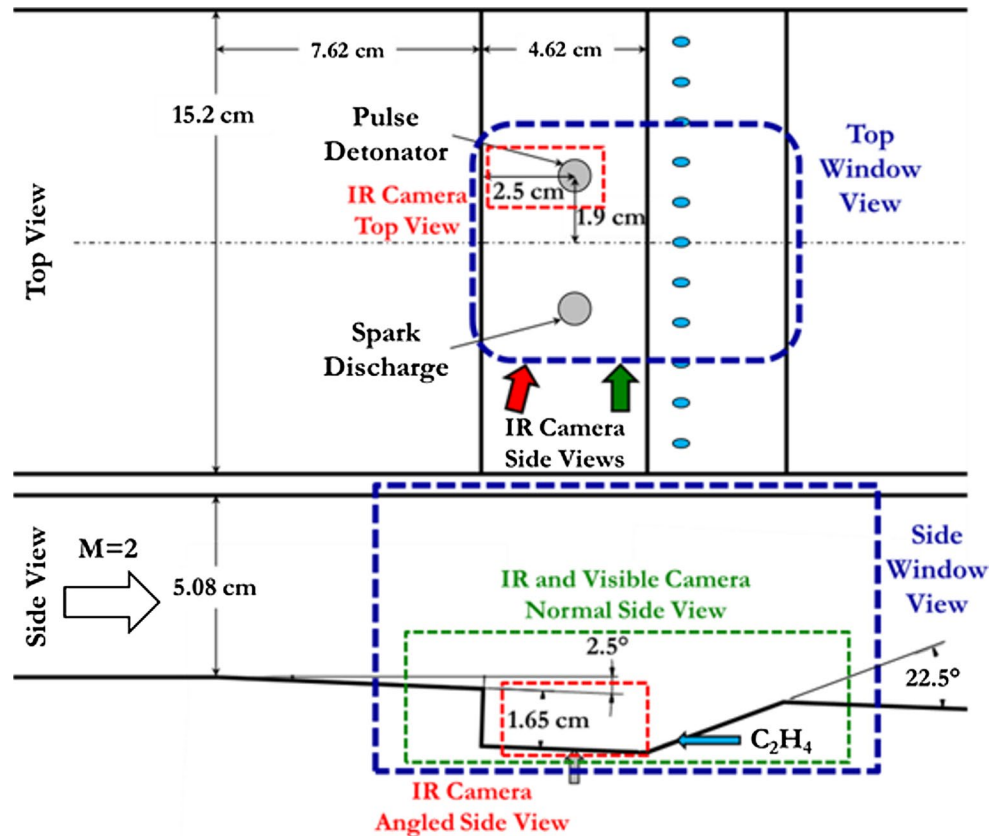
2 Experimental approach

2.1 Arrangement

Experiments were performed in the supersonic wind tunnel of Research Cell 19 at Wright-Patterson Air Force Base (Gruber and Nejad 1995). A generic cavity-based flameholder configuration was used, as illustrated in Fig. 1. The entire flow path was 15.2 cm wide, with a minimum height of 5.08 cm upstream of the cavity and a 2.5° divergence throughout the combustor. The cavity had a backward-facing step on the upstream side and a 22.5° ramp on the downstream. The cavity-based flameholder provides a subsonic recirculation zone to increase flow residence time, and therefore allows for flame stabilization that would not be possible in a pure supersonic flow. The burning cavity would therefore provide the piloting necessary for maintaining combustion in the supersonic flow. While there are many other flameholding techniques, cavities are commonly used and have been investigated extensively (Ben-Yakar and Hanson 2001; Gruber et al. 2001).The flow pattern created by the ramped cavity originates with the supersonic flow expanding over the front step of the cavity, producing a shear layer (see Fig. 2). The shear layer impinges upon the closeout ramp and is the region that separates supersonic from subsonic flow and allows for mass
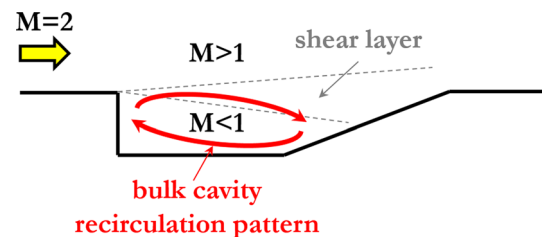

Fig. 2 Illustration of the bulk flowfield pattern within the cavity

exchange to and from the cavity. The bulk recirculation pattern produces a flow along the floor of the cavity that is opposite of the bulk supersonic flow direction.

Two ports were located at the base of the cavity, 1.9 cm off from the centerline. The ports accommodated both the spark discharge and PD ignition devices (Ombrello et al. 2015a). Fused silica windows formed the top and sides of the flow path near the cavity. Fuel (C_2H_4) was injected into the cavity through eleven holes toward the base of the cavity closeout ramp. Low global equivalence ratios were maintained in all experiments to ensure only burning in the cavity and no full-duct combustion. For the fueling rates of 40–200 standard liters per minute (slpm), the global equivalence ratio was 0.003–0.017. The cavity velocity flowfield was affected little across the range of fueling

rates. While the global equivalence ratio was low, the cavity equivalence ratio was much higher and changed during pre-ignition to quasi-steady burning because of the direct injection of fuel and the passive entrainment of air through the shear layer. Prior to ignition, the equivalence ratio was near stoichiometric, while the quasi-steady burning cavity was more rich. Nevertheless, since no measurements of the air entrainment into the cavity were performed, the fueling conditions are reported as the C_2H_4 flow rate (slpm) into the cavity for a relative perspective. A flow Mach number equal to 2, a total temperature of 600 K, and a total pressure near 485 kPa were used for all experiments. These conditions correspond to a flight Mach number of approximately 4.

Ignition was achieved using either a spark discharge or the PD. An automotive style exciter (AEM Model 30-2853) was used to provide up to 100 mJ/pulse of energy for the spark discharge, with a discharge duration of 3–4 ms. The PD provided a detonation plume with an excess of 100 J of sensible energy. The detonator was a 61 cm long and 1.03 cm inner-diameter stainless steel tube. The fuel and oxidizer injection as well as the spark igniter were at the closed end of the tube. The fuel (C_3H_8) and oxidizer (N_2O) were selected to produce detonations in the small diameter tube and at the low static pressure (approximately 62 kPa) in the cavity. Each firing produced a detonation wave near Chapman–Jouguet conditions, with wave speeds confirmed using ion probes near the exit into the cavity. The PD was operated at a 10 Hz repetition rate, with up to 10 pulses used for each cavity ignition study. Additional details are provided in refs. (Ombrello et al. 2015a, b).

Radiation intensity measurements were collected of spark discharges, detonation plumes, and quasi-steady burning within the cavity from both the top and side views of the tunnel. This allowed for sensitivities of the infrared imaging technique to be assessed for different times-scales in a windowed supersonic combustor. Additionally, broadband visible chemiluminescence was captured simultaneously through the side windows for some experiments to benchmark the infrared imaging technique.

2.2 Visible chemiluminescence measurements

A high frame-rate monochrome CMOS sensor camera (Photron FASTCAM SA-Z) was used to capture visible chemiluminescence from the quasi-steady burning cavity. The camera was positioned normal to the side windows of the tunnel (see Fig. 1). This allowed for simultaneous imaging of the visible chemiluminescence and infrared radiation, albeit from opposite sides of the tunnel. Imaging of the ignition transients with the spark discharge and the PD was performed during a previous set of experiments, when the infrared camera was not used. Nevertheless, images
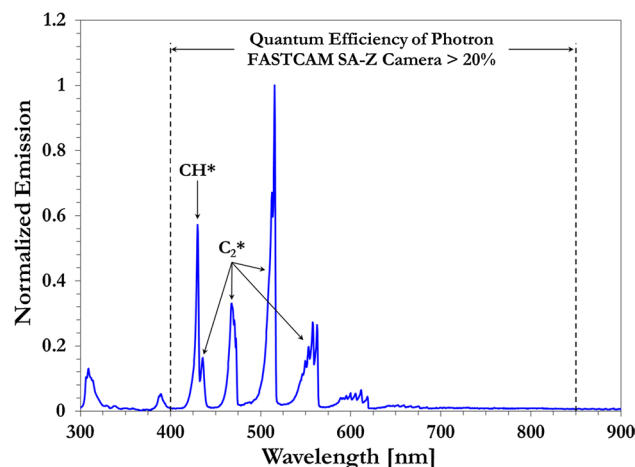

Fig. 3 Spectrum of normalized emission collected from quasi-steady burning flame in the cavity-based flameholder. Excited CH (CH*) and C_2 (C_2*) produce the most emission within the quantum efficiency band of 20 % or greater for the Photron FASTCAM SA-Z

were captured under the same set of conditions as transient radiation measurements, upon which strong repeatability had been documented (Ombrello et al. 2015a). A framing rate of 1000 frames per second (fps) was used for the quasi-steady burning cavity, while 50,000 fps was used for imaging the ignition processes with both the spark discharge and PD. Time-averaged results include 1000 time-resolved images. The sensor on the Photron FASTCAM SA-Z camera had greater than 20 % quantum efficiency between 400 and 850 nm, therefore capturing the entire visible spectral range, as well as some near-infrared. A plot of the typical normalized visible emission from a cavity-based flameholder burning C_2H_4 is shown in Fig. 3. The emission was captured using a fiber-coupled Ocean Optics Maya 2000 Pro spectrometer with 10 ms integration time. The spectrum showed that the main bands that the camera collected would be from CH* and C_2*.

2.3 Radiation intensity measurements

Two FLIR infrared cameras, an SC6700 and SC6800HD, were used to measure the radiation intensity emitted from top and side views of the cavity (respectively). The intensity measured by the cameras is described by the radiation transfer equation integrated between the spectral range of the detector and optics (Newale et al. 2015),

$$I = \int_{\lambda_1}^{\lambda_2} \alpha_\lambda I_\lambda(0)e^{-\tau_\lambda}d\lambda + \int_{\lambda_1}^{\lambda_2}\int_0^{\tau_\lambda} \alpha_\lambda I_{b\lambda}(\tau_\lambda^*)e^{-(\tau_\lambda + \tau_\lambda^*)}d\tau_\lambda^* d\lambda. \quad (1)$$

Here, the optical thickness is defined as,

$$\tau_\lambda = \int_0^s \kappa_\lambda ds, \quad (2)$$

and depends on the path length and the concentrations of the radiating species. Equation (1) neglects scattering by the radiating species and reflected or emitted radiation from the surroundings. α_λ accounts for transmission losses through the optics and window and variations in the spectral response of the detector. The camera used for measurements from the top of the cavity was sensitive between 1 and 5 µm, while the side camera was sensitive between 3 and 5 µm. In these spectral ranges, radiation emissions from the gases in the flow are primarily from H_2O (2.7 µm), C–H stretch (3.4 µm), and CO_2 (4.2 µm). The combustor windows (Corning 7980) absorb all infrared radiation between approximately 2.7 and 2.8 µm, while allowing approximately 90 % transmission near 3.4 µm. Near 4 µm, transmission decreases to approximately 10 %, with no transmission beyond approximately 4.3 µm. All values are for internal transmission at room temperature and for 10 mm window thickness (versus 19 mm and 29.7 mm for the top and side windows used, respectively), and consequently only provide a relative approximation of losses. Therefore, most of the radiation detected by the camera is attributed to emissions from the parent fuel (C_2H_4) or intermediate hydrocarbon fragments. As will be shown, this was consistent with observations made when narrowband filters were used. It is noted that no soot was ever observed in the experiments, either visibly or because of coating on combustor walls.

Infrared measurements were collected from two different side views (as illustrated in Fig. 1). A normal side view was used for imaging the quasi-steady cavity burning process, while a view angled slightly downstream was used for measurements of the PD plume because of limitations imposed by other diagnostic equipment. The normal view was used to collect measurements from the cavity and flow path, while the angled view was restricted to the cavity. For the top view, the infrared imaging was collected normal to the window.

The cameras were calibrated using a blackbody to quantify the radiation intensity. The distance between the blackbody and cameras matched the experiment, and the same window used in the tunnel experiments was included during the calibration. This approach for calibration approximated for transmission losses through the window and from room CO_2. The spectral response of the detector and transmission losses through the collection optics was considered for intensity measurements from the top. Thus, the reported radiation is what reached the detector. The spectral response of the camera from the side was not known, hence the reported radiation is approximately the radiation emitted from the flame. The difference in the approaches for the cameras is irrelevant for this effort because the intensity values between the two views were not compared for the analysis. It is important to note that what is reported for the time-resolved measurements is the difference between the radiation intensity emitted from the time-resolved images and the average intensity just prior to ignition being attempted. This allowed for radiation emissions from the flow to be analyzed while neglecting self-emission from the heated windows. This assumes that the temperature of the window does not vary notably during the time that average and time-resolved measurements are collected. In this study, this time was on the order of 10 ms; consequently, the temperature of the window was assumed to be constant. Moreover, it was assumed when subtracting time-resolved from average measurements that any changes caused by scattering are negligible. Average measurements of emissions from quasi-steady burning within the cavity included both emissions from the window and combustion process. Emissions from the gases were sufficient that they could be distinguished from emissions from the hot window.

The integration time on the cameras was set to values between 20 and 100 µs in an effort to optimize the sensitivity of the detector. The sampling frequency for the quasi-steady cavity burning was 190 fps, while 770 to 1450 fps were used for time-resolved measurements of the ignition process. The latter frequencies allowed for several consecutive measurements of ignition kernels and PD plumes to be collected.

2.4 Calculated species and temperature distribution

Numerical simulations were performed to provide interpretation of what was observed from the infrared radiation measurements for the quasi-steady burning cavity condition. Three-dimensional steady-state numerical simulations were conducted using Metacomps' CFD++ (Metacomp Technologies). For the simulations presented here, the nonlinear Harten–Lax–van Leer contact (HLLC) Riemann solver with a continuous total variation diminishing (TVD) limiter scheme was used to simulate the supersonic flow. Turbulence modeling was implemented using the nonlinear cubic k-epsilon Reynolds-Averaged Navier–Stokes (RANS) model, which can be used to account for normal-stress anisotropy, swirl, and streamline-curvature effects. An advanced two-layer wall function was applied to all wall surfaces, as it reduced the number of grids required. The turbulent Schmidt and Prandtl numbers were fixed at 0.75 and 0.9, respectively. Turbulent Schmidt numbers of 0.5 and 1.0 were also evaluated, but there were no significant differences in the results that impacted the comparison to the infrared radiation measurements. Chemical reactions were simulated using the TP2-reduced C_2H_4 kinetic mechanism including 22 species (H_2, H, O, O_2, OH, H_2O, HO_2,

H_2O_2, CH_3, CH_4, CO, CO_2, CH_2O, C_2H_2, C_2H_4, C_2H_6, C_2OH, C_2H_2O, CH_3CHO, C_3H_5, C_3H_6, N_2) and 206 reactions (Liu et al. 2006).

The computational domain consisted of the half-width and height of the test section with a total of 4.7 million cells. The grids were clustered near the walls with a $y+ < 52$. These grid dimensions were based upon previous grid methodologies, in which the first spacing away from the wall was 0.076 mm, and the stretching ratio was less than 1.2. This practice has shown that the grid resolution was sufficiently refined in terms of spatial convergence. A grid resolution study, including coarse and fine grid cells, was performed previously using the same geometry and similar conditions as the current experiment (Tam et al. 2013). The solution showed good agreement with the fine grid topology as well as the experimental data collected at that time. Note that the fine grid topology had the grid points doubled in each direction, while the coarse grid had half of the original grid mesh. Similar to the previous study (Tam et al. 2013), the numerical simulations were extended from the facility nozzle plenum to the entrance of the test section to provide the appropriate inflow conditions for the test section. This methodology obviates the use of ad hoc profiles at the test section entrance and allows for boundary layer growth.

3 Results and discussion

3.1 Quasi-steady cavity burning

3.1.1 Visible chemiluminescence

The time-averaged visible broadband chemiluminescence from the quasi-steady burning cavity is shown in Fig. 4 for cavity fueling rates of 40–200 slpm. These fueling rates created conditions within the cavity ranging from lean to fuel-rich burning. Visible broadband chemiluminescence predominately came from excited CH (CH*) and C_2 (C_2*) species produced during the reactions (see Fig. 3), and provided information about the burning flux. All chemiluminescence images have the same collection and intensity scale for ease in comparison. Note that the images were path-integrated, therefore making it difficult to interrogate the spanwise structure of the burning. Nevertheless, the radiation intensity measurements were path-integrated as well, therefore providing a good means for comparison. For 40 slpm, there was a weak shear layer flame, with the majority of the burning flux occurring in the base of the center of the cavity. As the fueling rate was increased to 55 slpm, the burning flux in the shear layer increased, with diminished burning in the base of the cavity. For 75 and 90 slpm, the burning flux in the shear layer moved downstream until at 150 slpm, there was concentrated burning
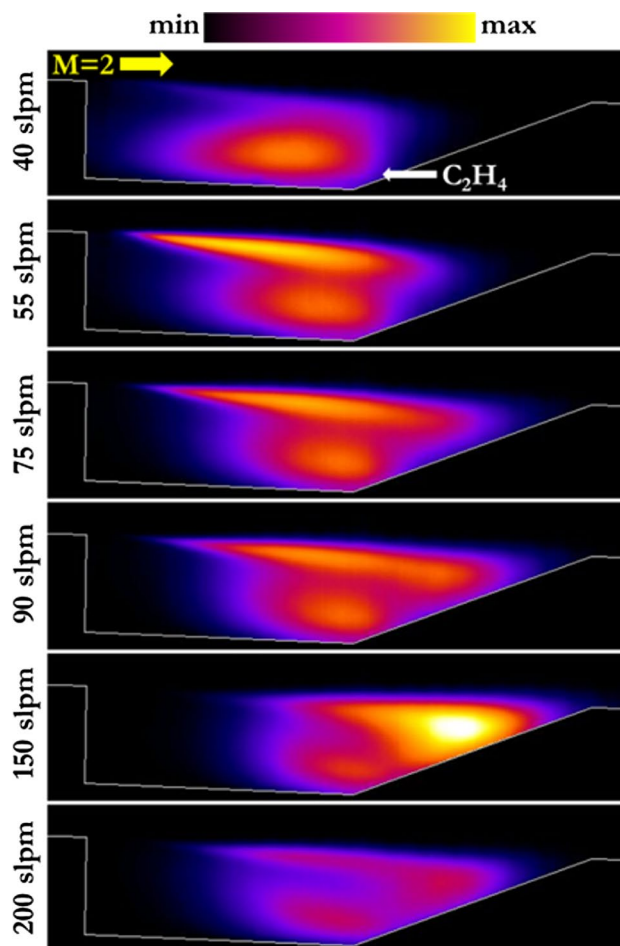

Fig. 4 Time-averaged visible broadband chemiluminescence of quasi-steady cavity burning from side view for fueling rates from 40 to 200 slpm. An artificial look-up table was used and consistently applied to each image for enhanced contrast

on the cavity closeout ramp. With increased fueling rate to 200 slpm, the cavity burning changed dramatically with significantly decreased intensity and slight shift of burning flux toward the front step of the cavity. Note that similar to the 40 slpm case, the 200 slpm case had decreased burning flux compared to the intermediate fueling rates, indicating that the upper bound of cavity burning (blowout) was being approached. The results of the visible broadband chemiluminescence in Fig. 4 are important because it showed how burning within the cavity varied for different fueling rates. Consequently, shifts in infrared emissions were expected because of the dependence of radiation on the temperature and species concentrations.

3.1.2 Infrared radiation emissions

Measurements of radiation emissions (reported as photon counts) from flames within the cavity are shown in Fig. 5

Fig. 5 Radiation emissions emitted from the side for quasi-steady burning for fueling rates of 55, 75, and 90 slpm. The measurements include emissions from both the window and the gases
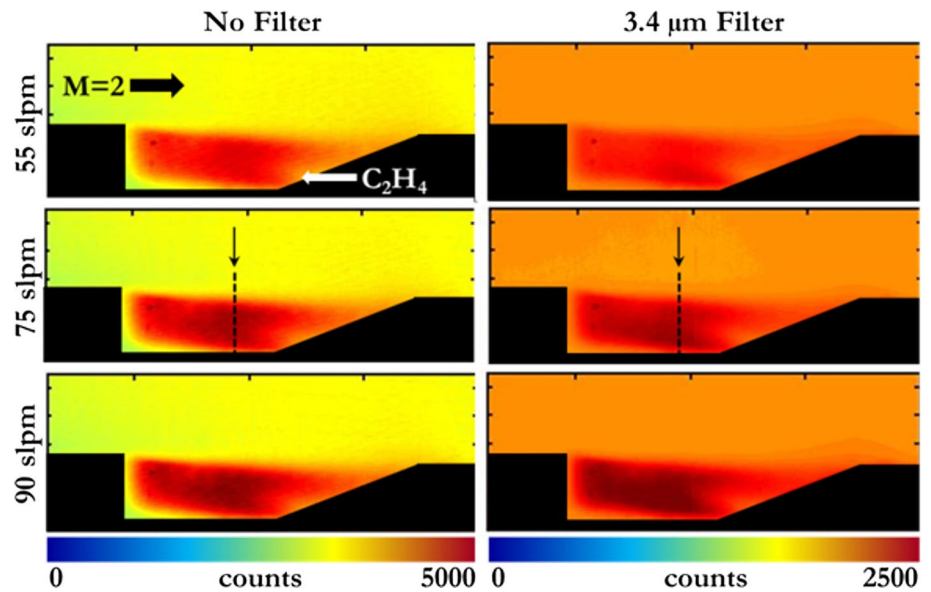
for fueling rates from 55 to 90 slpm. Measurements collected at the other fueling conditions corresponding to chemiluminescence are not reported because radiation emissions from the heated windows of the combustor masked radiation emissions from the gases. The left panel of Fig. 5 shows results when no filter was used with the infrared camera, while the right panel shows those when a narrowband filter centered on 3.4 μm was used. These measurements provide insight into the distributions of reactants, combustion intermediates, and products, and can be used for evaluating simulations [e.g., (Blunck et al. 2012a; Rankin et al. 2015)]. It is apparent that the burning flux (visible chemiluminescence) shown in Fig. 4 and the radiation emissions in Fig. 5 have different distributions throughout the cavity. For the infrared emissions, there was a fairly uniform distribution throughout the cavity and an increase in emissions with increased fueling rate. Radiation emissions from the shear layer were not evident. Two different narrowband filters, centered near 3.4 and 4.2 μm, were used with the camera to establish the dominant spectral bands of infrared emissions. With the 4.2 μm filter (not shown), no emission from inside the cavity was measured. This was expected because the fused silica windows had minimal transmission (on the order of several percent) at 4.2 μm. This showed that radiation emissions without the filter were not from CO_2. When using the 3.4 μm filter, the images showed emission throughout the cavity, similar to the results without a filter. Additionally, the emission increased with increased fueling rates with or without the filter being used. To provide a more quantitative comparison, line plots are shown in Fig. 6 of the normalized emissions for the 75 slpm case at the streamwise location illustrated by the dashed lines. The two profiles agreed well, further indicating that the majority of the emission shown
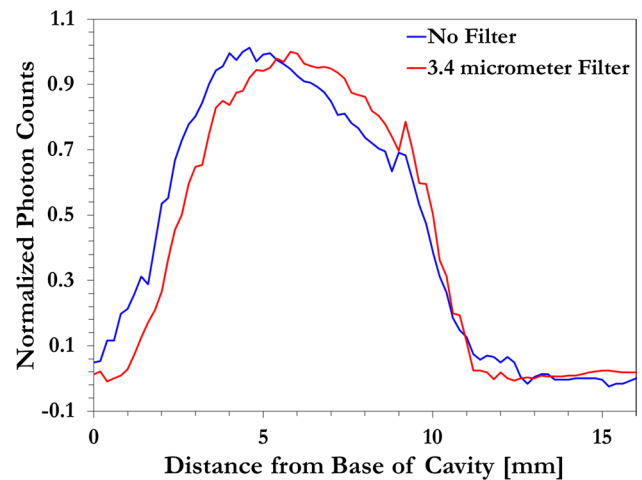

Fig. 6 Normalized line profiles of the radiation intensity in the cavity for the lines marked in the unfiltered and filtered measurements shown in Fig. 5 for a fueling flow rate equal to 75 slpm

in the unfiltered images was emitted at wavelengths near 3.4 μm. Consequently, radiation emissions are attributed to emissions from the parent fuel (C_2H_4) and intermediate hydrocarbon fragments; the C–H stretch in hydrocarbons has strong emission near 3.4 μm. This explains why emissions from the chemiluminescence tend to be closer to the ramp and in the shear layer and the peak infrared emissions tend to be closer to the step. The latter occurs because the cavity tends to have richer equivalence ratios near the step because of being a lower speed region downstream of where fuel is introduced. The former observation of the chemiluminescence occurred because the fuel breaks down and completes oxidation in the shear layer and near the ramp.

3.1.3 Simulations of quasi-steady cavity burning

Simulations were performed of the quasi-steady burning cavity at different fueling rates to provide insights into the temperature and species distributions. Figure 7 presents the temperature and the distribution of combustion species with mole fractions greater than 0.001 for the 75 slpm of fuel condition. Only at these mole fractions would infrared radiation emissions be expected to quantifiably contribute to the unfiltered measurements, because of the dependence of the radiative transfer equation on concentration. Consequently, only the species distributions reported could contribute to the unfiltered radiation intensity measurements. The plots are a series of streamwise slices averaged across the span of the cavity in order to provide an average view from the side for comparison to the imaging (top panel). The three major hydrocarbon species present were
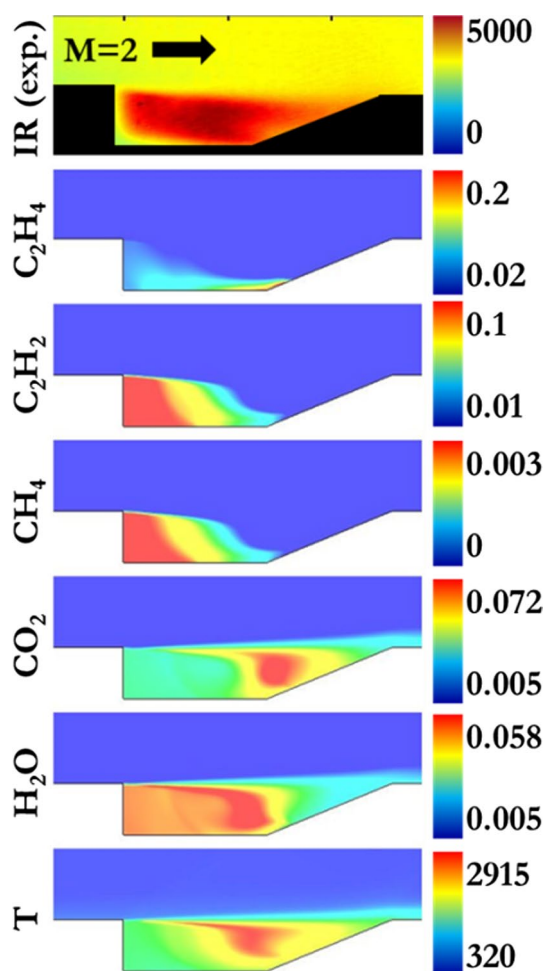

Fig. 7 Calculated species and temperature distribution in a quasi-steady burning cavity at a fueling rate of 75 slpm. The scale to the right of the images denotes counts, mole fraction, and Kelvin, for the infrared measurements (*top*), species concentrations (*middle*), and temperature (*bottom*), respectively

the parent fuel (C_2H_4), C_2H_2, and CH_4. Peak C_2H_4 was observed along the base of the cavity, as expected because of the fuel injection at the base of the ramp. The C_2H_2 and CH_4 had similar distributions, with the largest concentrations near the front step of the cavity. Relatively high-radiation emissions were observed in this region. Near the cavity closeout ramp a discrepancy between the hydrocarbon distribution and infrared measurements was observed: low concentrations of species but relatively high-radiation emissions. Note, however, that the infrared radiation depended on both the concentration and the temperature. Consequently, while the concentration was lower in this region the higher temperatures near the ramp caused higher radiation emissions. Water vapor was the other potential species whose distribution could correspond to the infrared images. However, this was not the case in this experiment because the window absorbed all radiation emissions near the spectra at which water vapor emitted.

Contour plots of the summation of all the hydrocarbon species for fueling rates of 55, 75, and 90 slpm are shown in Fig. 8 (top) along with the corresponding temperature distribution (bottom). The concentrations of the primary hydrocarbons locally were combined for analysis, in consideration that each of the species could contribute to infrared emissions from C–H stretch. There was a noticeable increase in hydrocarbon concentration and temperature with increased fueling rate, as expected and noted in the infrared images in Fig. 5 by increases in peak intensity. While the calculations did not provide a direct comparison since the radiation was not simulated, it did show that the flow features and distribution of species and temperature were correctly captured by the infrared imaging technique. With different window material and narrowband filters, radiation emissions from specific species can be targeted.

3.2 Transient ignition process

With the confidence gained in applying infrared measurements for quasi-steady cavity burning, the next step was to extend the technique to investigate transient processes, such as ignition within the cavity. The entire process from energy deposition to a quasi-steady burning cavity was on the time-scale of approximately 3–12 ms, for the ignition techniques evaluated. This highly transient process was particularly challenging to interrogate considering the sensitivities needed to measure a large dynamic range process, from weakly burning to robust combustion. Infrared imaging was applied to capture the initial ignition event for two energy deposition devices. This included tracking of ignition kernels shed from a spark discharge in the base of the cavity and the plume of a detonation from a pulse detonator. The latter was highly disruptive to the flow field within the cavity, which was evident in measurements.
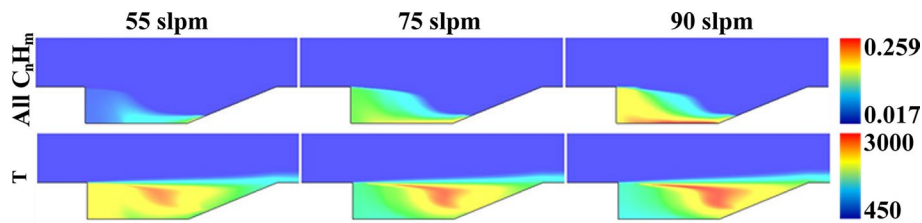
Fig. 8 Calculated average hydrocarbon and temperature distribution in a quasi-steady burning cavity at fueling rates of 55, 75, and 90 slpm. The scale to the right of the images denotes the mole fraction and Kelvin for the combination of all hydrocarbons (C_nH_m) and temperature, respectively

3.2.1 Spark discharge ignition

Radiation intensity measurements were collected of emissions from kernels which formed from spark discharges, and then propagated within the cavity. Similar measurements have been reported by Blunck and co-workers and Okhovat (Blunck et al. 2012c; Okhavat 2015) for quiescent conditions, but never for measurements through a warm window in a high-speed flammable mixture. The pockets of hot gas formed from the sparks had very weak chemiluminescence because of the relatively small quantity of heat release; therefore, these measurements provided a good assessment of the sensitivity of the infrared imaging. A comparison of infrared and chemiluminescence imaging of spark kernels is shown in Fig. 9. The infrared and chemiluminescence measurements were of different spark events and should not be compared directly; comparison should be made of the structures observed throughout the ignition process. The separation time was roughly 0.7 ms for the infrared images (a)–(d) in Fig. 9. Therefore, no correlation between images with regard to the shedding kernels could be achieved. For the chemiluminescence, each image (e)–(h) was only separated by 0.08 ms and, therefore, showed the time-resolved kernel shedding process. Plasma discharge and the hot igniter tip were evident near the top of the images as the highest intensity. Downstream

of the igniter (i.e., bottom of images) localized pockets of emission in the infrared and visible was observed. Multiple regions with higher radiation intensity in the same image indicated a shedding like phenomena of the kernels. The radiation intensity measurements showed that the mixture temperature was elevated in multiple discrete regions, in consideration of the strong dependence of radiation intensity on temperature. The shedding phenomena occurred because the spark discharge duration was relatively long in comparison to the local flow residence time (average cavity cycling time of 1–2 ms with a velocity on the order of 10–100 m/s at the electrodes). The spark discharge was present for 3–4 ms, creating a high-temperature plasma channel. As the flow in the base of the cavity interacted with the high-temperature plasma channel, pockets of elevated temperature gas were created in its wake. The radiation intensity measurements showed that regions of higher temperature could be distributed on either side of the igniter and may not be connected downstream. One or more of these elevated temperature regions were what typically led to ignition within the cavity flameholder (Ombrello et al. 2015a). In future work, estimates of the temperature of the kernels could be determined from radiation intensity measurements for non-reacting conditions (from emissions from CO_2 or H_2O in the air) [e.g., (Blunck et al. 2012c; Okhavat

Fig. 9 Infrared imaging (*top panels*) and chemiluminescence imaging (*bottom panels*) of the base of the cavity through the top window of spark discharge ignition with a fueling rate equal to 75 slpm. Infrared and chemiluminescence measurements were of different spark events. The time between each infrared image was roughly 0.7 ms, while for each chemiluminescence image was 0.08 ms
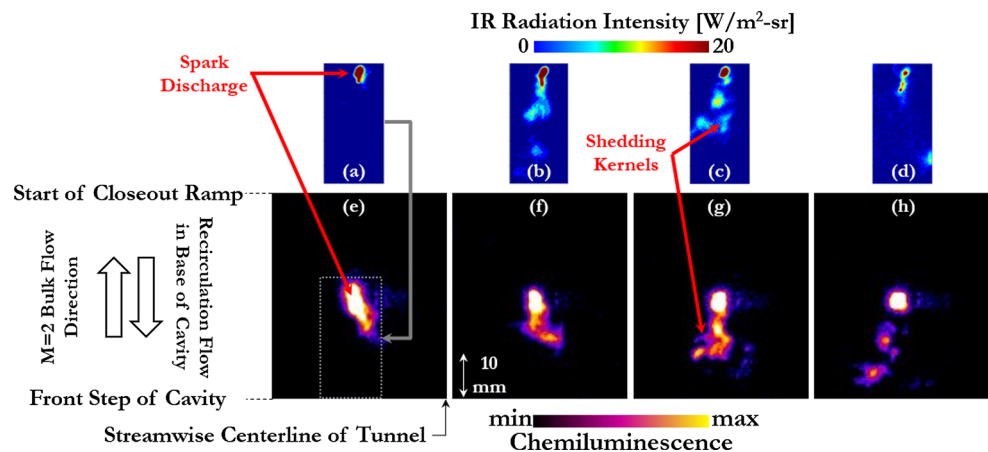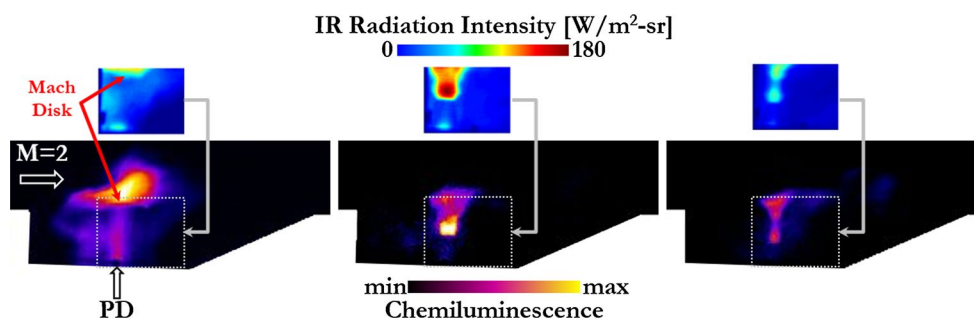
Fig. 10 Infrared (*top*) and chemiluminescence imaging (*bottom*) of early stages of ignition by PD exhausting into the cavity with a fueling rate of 75 slpm. Infrared and chemiluminescence measurements were of different PD events, but have the same scale. The time between each infrared and chemiluminescent and image was approximately 0.7 ms

et al. 2016)] now that the viability of such measurements have been established.

3.2.2 PD ignition

Representative radiation intensity measurements and chemiluminescence images of consecutive stages of detonation plumes entering the cavity are shown in Fig. 10. Note that the infrared and chemiluminescence images are for different pulse detonation events, and that infrared measurements were collected for an off-angle view (see Fig. 1) because of experimental limitations. Three specific portions of the early stage of the ignition process were evident in the radiation intensity measurements and chemiluminescence images. The first was the initially highly underexpanded plume with a large barrel shock terminating in a large Mach disk in the upper portion of the shear layer (left panels). This was evident in the top of the images by the horizontal region of elevated emission, which is the Mach disk. The second was when the Mach disk was located below the shear layer and within the fueled cavity as the barrel shock decayed (middle panels). Lastly, the shock diamonds were observed as the pressure in the detonation tube decreased throughout the blowdown process to static pressure conditions (right panels). The multiple stages of the PD exhaust process shown in Fig. 10 are vital to understanding cavity ignition with this device. The initial highly underexpanded portion of the pressure pulse (left panels) forced larger regions of mixing of the fuel and air and elevating the temperature. This can be detrimental by altering the normal cavity cycling that may lead to failed ignition attempts (Ombrello et al. 2015a). After the initial stage of the detonation emerging into the cavity in the left panels, the jet underexpansion diminished, and the high-temperature exhaust from the PD was dumped into the cavity, which served as the main ignition source.

Radiation emissions from the PD plume were compared between failed and successful cavity ignition events to investigate the cause of ignition or non-ignition for the same flow conditions. One specific example of where cavity ignition could be intermittent was at a fueling rate of 75 slpm. This condition was at the limit of where the PD could successfully ignite the cavity because of the disruption to the cavity fueling and burning from the detonation exhaust (Ombrello et al. 2015a; Miller et al. 2016). The PD was typically fired for 1 s at 10 Hz to attempt ignition. At the 75 slpm cavity fueling rate, multiple pulses were required prior to achieving ignition in the cavity. It was observed that the peak radiation intensity emitted by the plumes increased with each successive firing of the PD. When the experiments were repeated shortly thereafter for the same operating conditions a single detonation plume achieved ignition. In the corresponding infrared image, combustion within the cavity was evident as well as the detonation plume. The peak radiation intensity emitted from the flame and the plume exceeded that corresponding to the previous sequence of PD firings (without ignition). These findings suggest that the temperature of the plume, which the radiation intensity depends upon, has a direct effect on ignition and that the temperature of the plumes increased with multiple pulses. The increase in temperature could occur because of decreased heat losses from the detonation to the walls of the PD. The wall temperature rises rapidly with a detonation and cannot equilibrate through wall conduction in the inter-pulse time, leading to less heat loss with successive pulses. The post-detonation products that remain in the tube and are exhausted into the cavity therefore increased in temperature with each pulse until ignition was achieved.

The hypothesis that the radiation intensity measurements show an increase in temperature between successive firings of the PD was further evaluated using the same PD with a high-frequency pressure transducer (PCB Piezotronics) placed near the tube exit. Pressure measurements normalized to the peak value achieved for the first pulse are shown in Fig. 11. For a burst of pulses, the maximum pressure and the blowdown time remained constant within
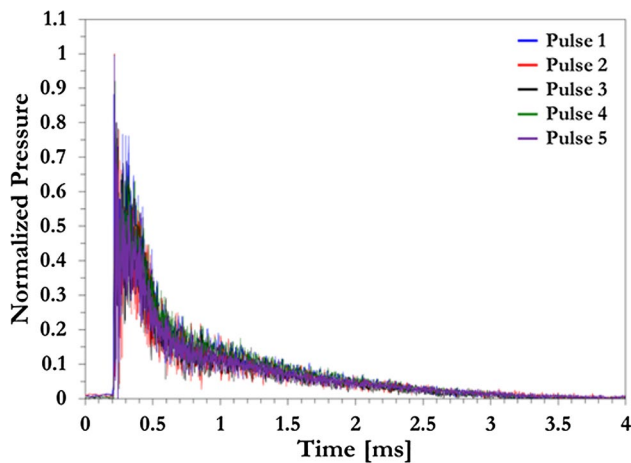
Fig. 11 Pressure versus time measured near the exit of the PD for a burst of pulses

the uncertainty of the measurements. Therefore, the pressure pulse and fluid dynamics of the detonation plume did not change as a function of pulses. The remaining factor that could affect cavity ignition would be the detonation plume temperature and the species concentrations. From a first order, the temperature would be the driving factor in whether ignition would be achieved, while the composition would lead to further enhancement. In summary, both the radiation intensity and pressure measurements show that the sensitivity of cavity ignition to the sequence of PD firing was caused by changes in plume temperatures. Therefore, heat loss and plume temperature should be considered when a PD is used to ignite a high-speed flow.

4 Summary

The utility of infrared thermography for studying high-speed transient and steady-state combustion processes in a windowed combustor has been evaluated for the first time by collecting measurements in a Mach 2 cavity-based flameholder. The majority of the infrared radiation was from C–H stretch, based on measurements and analysis of quasi-steady burning. The results illustrated the ability to use this tool to provide guidance into the hydrocarbon and temperature distribution within the cavity. This was supported by comparison to numerical simulations of the cavity burning process. The distribution of other radiating species (e.g., CO_2, CO, H_2O) can be determined using appropriate filters and windows. The utility of using radiation intensity measurements to interrogate transient ignition processes was explored by measuring the radiation intensity emitted from spark discharge and pulse detonation plumes. Ignition kernels from a simple spark discharge were readily measured. Shedding of high-temperature regions from

the spark discharges was evident, as expected because of fluid mechanic interactions. The shedding of these regions affects ignition. The exhaust from a pulse detonator was captured with imaging of the barrel shock, Mach disk, and overall exhaust process. Comparison of the radiation intensity indicated that the temperature of the plume increased with consecutive firings. This explained the higher probability of cavity ignition with consecutive firings. This study shows that infrared radiation measurements are feasible in the windowed combustion environments and can be interrogated to provide insights into the dynamic fluid and combustion processes.

References

Allen M, Parker T, Reinecke W et al (1993) Fluorescence imaging of OH and NO in a model supersonic combustor. AIAA J 31:505–512

Ben-Yakar A, Hanson R (2001) Cavity flame-holders for ignition and flame stabilization in scramjets: an overview. J Propuls Power 17:869–877

Blunck D, Basu S, Zheng Y et al (2009) Simultaneous water vapor concentration and temperature measurements in unsteady hydrogen flames. Proc Combust Inst 32:2527–2534

Blunck D, Harvazinski M, Merkle C, Gore J (2012a) Influence of turbulent fluctuations on the radiation intensity emitted from exhaust plumes. AIAA J Thermophys Heat Transf 26:581–589

Blunck D, Harvazinski M, Rankin B et al (2012b) Turbulent radiation statistics of exhaust plumes exiting from a subsonic axisymmetric nozzle. J Thermophys Heat Transf 26:286–293. doi:10.2514/1.T3621

Blunck DL, Kiel BV, Goss L, Lynch A (2012c) Spatial development and temperature of spark kernels exiting into quiescent air. J Propuls Power 28:458–465. doi:10.2514/1.B34131

Brown, M., Herring, G., Cabell K, Hass N, Barhorst T, Gruber M (2012) Optical measurements at the combustor exit of the HIFiRE 2 ground test engine. In: 50th AIAA Aerospace Sciences Meeting. Nashville, TN, pp AIAA-2012-0857

Busa K, Rice B, McDaniel J et al (2015) Direct measurement of combustion efficiency of a dual-mode scramjet via TDLAT and SPIV. In: 53rd AIAA Aerospace Sciences Meeting2. Kissimmee. FL, pp AIAA-2015-0357

Chuah KH, Saito K, Hashiba Y et al (2016) A spectrally resolved imaging method for investigating alcohol pool fires. Combust Sci Technol 188:277–289. doi:10.1080/00102202.2015.1103232

Cutler A, Magnotti G, Cantu L et al (2014) Dual-pump coherent anti-stokes Raman spectroscopy measurements in a dual-mode scramjet. J Propuls Power 30:539–549

Do H, Cappelli M, Mungal M (2010) Plasma assisted cavity flame ignition in supersonic flows. Combust Flame 157:1783–1794

Gauba G, Klavuh K, McDaniel J et al (1997) OH planar laser-induced fluorescence velocity measurements in a supersonic combustor. AIAA J 35:678–686

Gross KC, Bradley KC, Perram GP (2010) Remote identification and quantification of industrial smokestack effluents via

imaging Fourier-transform spectroscopy. Environ Sci Technol 44:9390–9397

Gruber M, Nejad A (1995) New supersonic combustion research facility. J Propuls Power 11:1080–1083

Gruber M, Baurle R, Mathur T, Hsu K (2001) Fundamental studies of cavity-based flameholder concepts for supersonic combustors. J Propuls Power 17:146–153

Gruber M, Donbar J, Carter C, Hsu K (2004) Mixing and combustion studies using cavity-based flameholders in a supersonic flow. J Propuls Power 20:769–778

Hammack S, Lee T, Hsu K, Carter C (2013) High-repetition-rate OH planar laser-induced fluorescence of a cavity flameholder. J Propuls Power 29:1248–1251

Lee P, McMillin B, Palmer J, Hanson R (1992) Planar fluorescence imaging of a transverse jet in a supersonic crossflow J Propuls Power 8:729–735

Liu J, Tam CJ, Law C (2006) Simulations of cavity-stabilized flames in supersonic flows using reduced chemical kinetic mechanisms. In: 42nd joint propulsion conference, Sacramento, CA, pp 2006–4862

Metacomp Technologies Metacomp Technologies (2009). http://www.metacomptech.com/index.html. Accessed 1 Jan 2009

Miller J, Peltier S, Slipchemnko M, et al (2016) Investigation of transient ignition processes in a model scramjet pilot cavity using simultaneous 100-kHz formaldehyde planar laser-induced fluorescence and CH* chemiluminescence imaging. In: Proceedings of the Combustion Institute (in review)

Modest M (2003) Radiative heat transfer, 2nd edn. Academic Press, New York

Newale AS, Rankin BA, Lalit HU et al (2015) Quantitative infrared imaging of impinging turbulent buoyant diffusion flames. Proc Combust Inst 35:2647–2655. doi:10.1016/j.proci.2014.05.115

Okhavat S (2015) Temperature evolution of spark kernels in quiescent and cross-flow conditions. Oregon State University, Corvallis

Okhavat S, Hauth J, Blunck D (2016) Temperatures of spark kernels discharging into quiescent or cross-flow conditions. J Thermophys Heat Tr. doi:10.2514/1.T4927

Ombrello T, Carter C, Tam C, Hsu K (2015a) Cavity ignition in supersonic flow by spark discharge and pulse detonation. Proc Combust Inst 35:2101–2108

Ombrello T, Carter CD, McCall J et al (2015b) Enhanced mixing in supersonic flow using a pulse detonator. J Propuls Power 31:505–512

Peltier S, Carter C (2015) Response of a Mach 3 cavity flameholder to a shock-induced distortion. In: 53rd AIAA Aerospace Sciences Meeting, pp 2015–0883

Rankin BA, Magnotti G, Barlow RS, Gore JP (2014) Radiation intensity imaging measurements of methane and dimethyl ether turbulent nonpremixed and partially premixed jet flames. Combust Flame 161:2849–2859. doi:10.1016/j.combustflame.2014.04.019

Rankin BA, Ihme M, Gore JP (2015) Quantitative model-based imaging of mid-infrared radiation from a turbulent nonpremixed jet flame and plume. Combust Flame 162:1275–1283. doi:10.1016/j.combustflame.2014.10.019

Rasmussen C, Driscoll J, Hsu K et al (2005) Stability limits of cavity-stabilized flames in supersonic flow. Proc Combust Inst 2:2825–2833

Rasmussen C, Dhanuka S, Driscoll J (2007) Visualization of flame-holding mechanisms in a supersonic combustor using PLIF. Proc Combust Inst 31:2505–2512

Rhoby MR, Blunck DL, Gross KC (2014) Mid-IR hyperspectral imaging of laminar flames for 2-D scalar values. Opt Express 22:21600. doi:10.1364/OE.22.021600

Ryan M, Gruber M, Carter C, Mathur T (2009) Planar laser-induced fluorescence imaging of OH in a supersonic combustor fueled with ethylene and methane. Proc Combust Inst 32:2429–2436

Tam C, Hsu K, Hagenmaier M, Raffoul C (2013) Studies of inlet distortion in a direct-connect axisymmetric scramjet isolator. J Propuls Power 29:1382–1390

Tuttle S, Carter C, Hsu K-Y (2014) Particle image velocimetry in a nonreacting and reacting high-speed cavity. J Propuls Power 30:576–591